

Experimental investigation of turbulent wave boundary layers under irregular coastal waves

Jing Yuan^a, Sunil Manohar Dash^a

^a*Department of Civil and Environmental Engineering, National University of Singapore,
1 Engineering Dr. 2, Block E1A 07-03, Singapore 117576*

Abstract

In this study full-scale experiments of wave boundary layers under irregular coastal waves are conducted using an oscillatory water tunnel. The flow conditions cover two rough bottoms, three types of wave shapes, i.e. sinusoidal, skewed and asymmetric waves, and two types of irregular-wave sequences. The instantaneous turbulent velocity fields are measured with a 2-dimensional Particle Image Velocimetry system. The measured turbulence statistical values show that the residual turbulence at the end of wave cycle can persist into the next wave cycle, until the next cycle's self-produced turbulence becomes sufficiently strong. Consequently, the Reynolds-averaged flow at the beginning of a wave cycle can behave as if the flow "memorizes" the previous wave cycle. However, this memory effect quickly vanishes, and therefore does not have a significant influence on some key boundary layer characteristics, e.g. bottom shear stress. For irregular wave boundary layers with skewed and asymmetric free-stream velocities, the measured mean current and the associated mean bottom shear stress confirm the existence of a well-known boundary layer streaming due to the imbalance of turbulence between the two halves of a wave cycle, and the measurements of bottom shear

stress of individual waves closely resemble those for periodic-wave conditions. These experimental results suggest that modeling irregular wave boundary layers in a wave-by-wave manner is plausible.

Keywords: irregular waves, Turbulent wave boundary layer, Oscillatory Water Tunnel, Bottom shear stress, Laboratory experiment

1. Introduction

In the coastal environment, shoaling waves interact with the underneath seabed through a thin turbulent wave boundary layer (WBL), which plays an important role in determining coastal sediment transport. If the wave length is much longer than the excursion amplitude of the bottom wave orbital motion, local WBLs can be approximated by oscillatory boundary layer flows, which are uniform in the bottom-parallel direction, so prototype flow conditions can be easily achieved in oscillatory water tunnels (OWT). A number of early OWT studies, e.g. Jonsson and Carlsen (1976), Sleath (1987) and Jensen et al. (1989), revealed some key characteristics of WBL and provided valuable measurements for developing or validating predictive models (e.g. Grant, 1977; Justesen, 1988), but they only considered sinusoidal oscillatory flows, which will produce a zero net sediment transport rate over a horizontal seabed.

Coastal waves become increasingly nonlinear as they approach the shore, which leads to two nonlinear features differentiating the two half-periods of the wave bottom orbital velocity, i.e. skewness (the velocity time series has peaked crest and flat trough) and asymmetry (the velocity time series becomes forward-leaning). As a result, the intra-period variation of bottom

shear stress exhibits similar features. A number of simple estimators have been proposed to predict the bottom shear stress for skewed and/or asymmetric periodic WBLs, e.g. Gonzalez-Rodriguez and Madsen (2007) and Abreu et al. (2013). Generally speaking, positive skewness and asymmetry lead to larger bottom shear stress under the crest half-cycle, so a net positive (usually onshore) bedload transport rate should be expected, since bedload sand grains can immediately react to the varying bottom shear stress in a quasi-steady manner. This is confirmed by a number of coarse-sand OWT studies in the sheet-flow regime, e.g. Ribberink and Al-Salem (1995) and O'Donoghue and Wright (2004) for flow skewness, van der A et al. (2010) and Ruessink et al. (2011) for flow asymmetry. However, it is also observed that in some fine-sand OWT tests the phase-lag effect, i.e. suspended fine particles cannot immediately settle back to the movable bed at the moment of flow reversal, can reduce the onshore net transport rate or even lead to a net offshore transport rate. Some OWT studies also reveal another important feature of WBLs with skewness and asymmetry, i.e. a boundary layer streaming in the negative (usually offshore) direction (e.g. Ribberink and Al-Salem, 1995; van der A et al., 2011). A number of analytical and numerical models (e.g. Trowbridge and Madsen, 1984; Holmedal and Myrhaug, 2006; Kranenburg et al., 2012; Yuan and Madsen, 2015) have illustrated that this streaming (hereafter referred to as the TI (turbulence-imbalance) streaming) is due to the imbalance in flow turbulence between the two half-cycles, so it is different from another well-known wave boundary layer streaming (LH-streaming hereafter) first proposed by Longuet-Higgins (1953), which is driven by a net downward transfer of momentum due to the fact that the

horizontal and vertical wave orbital velocities in the close vicinity of the bed are not 90° out of phase. Many OWT and large-flume experimental studies have shown that the streaming-related net sediment transport rate can be quite substantial, so a few numerical or analytical models are established to investigate the influence of TI- and LH-streamings on net sediment transport rate (e.g. Ruessink et al., 2009; Holmedal and Myrhaug, 2009; Fuhrman et al., 2013; Kranenburg et al., 2013).

The real coastal waves are always irregular, so a big question is how to extend the existing periodic-wave-based knowledge and predictive models to irregular-wave scenarios. Although some numerical models can directly simulated boundary layer flows under a train of irregular waves (e.g. Holmedal et al., 2003; Tanaka and Samad, 2006), this approach is still too computationally expensive for practical applications. In the literature two major approaches are commonly adopted to realize the extension, i.e. the probabilistic and the representative-wave approaches. The latter simply conceptualizes the irregular waves as a representative periodic wave. Madsen (1994) analytically showed that a periodic wave with its amplitude and period being the root-mean-square (RMS) velocity and average period of the irregular wave bottom orbital motion, respectively, can be used for modeling irregular wave-current boundary layers. This model is recently validated by the OWT experiment of Yuan (2016). The representative wave for modeling sediment transport is rather arbitrarily defined. For example, van der A et al. (2013) proposed to use the significant amplitude and the peak spectral period of wave bottom orbital velocity in their formula for net sediment transport rate under non-breaking waves and currents, which is calibrated

mostly based on periodic-wave experiments. It can be hypothesized that different representative waves should be adopted for different boundary layer or sediment transport processes, so more research effort is required to further improve the representative-wave approach. The probabilistic (or wave-by-wave) approach treats irregular waves as a set of independent periodic waves following a certain probability distribution, so existing periodic-wave-based models can be directly applied to yield the probability distributions for some physical quantities of interest, e.g. net sediment transport rate. Myrhaug (1995) followed by Myrhaug et al. (2001) adopted this method to obtain the probability distribution of the maximum wave bottom shear stress under waves or wave-current flows with the assumption that the wave motion is a stationary Gaussian narrow-band random processes. The same principle has been adopted for modeling bedload transport under wave-current flows (Holmedal and Myrhaug, 2004) and sediment suspension under the influence of skewed and asymmetric bottom shear stress and LH-streaming (Myrhaug et al., 2015). The advantage of the probabilistic approach is that it can rigorously account for the difference among individual waves, e.g. each wave can have its own skewness and asymmetry. However, this approach assumes that a wave can be modeled as being in a periodic wave train, which may not be suitable for some boundary layer processes that cannot react immediately to the change of wave condition. It can be argued that WBLs may have some “memory”, i.e. some residual influence of a wave cycle will persist into the next wave cycle. This memory effect makes waves within a irregular wave train not truly independent, and therefore undermines the probabilistic approach. Should these concerns be cleared with full-scale experimental

evidences, the probabilistic approach will be a powerful tool, which can be used in developing or verifying the representative-wave approach (e.g. Yuan and Madsen, 2010).

Very few experimental studies of turbulent boundary layers under irregular waves are available in the literature. Simons et al. (1994) directly measured bottom shear stress under irregular waves plus currents using shear plates in their wave-basin experiments. Chassagneux and Hurther (2014) conducted a flume experiment of wave boundary layer under irregular breaking waves over a movable bed. These small scale experiments provide some insights to the bottom shear stress and the flow structure of irregular wave boundary layers. Bhawanin et al. (2014) reported a full-scale OWT studies of irregular wave boundary layers over fixed rough beds. Their irregular waves were generated by amplitude-modulating a train of periodic waves, so the memory effect can be studied by comparing tests with different modulations. Their experimental results suggest that the memory effect is probably negligible in the near-bottom region, but are not totally absent at higher levels from the bed. They suggested that more experimental work with detailed measurements of boundary layer flows and bottom shear stress is still required to further elucidate the memory effect. It is also unclear whether and how wave irregularity affects the bottom shear stress and the TI-streaming of irregular WBLs with skewed and asymmetric free-stream velocities.

In this study full-scale experiments of irregular turbulent wave boundary layers are conducted over fixed rough bottoms in an OWT. The main objectives are (1) to study the memory effect on key wave boundary layer physics and (2) to investigate how wave irregularity influences the bottom

shear stress and the TI-streaming of skewed and asymmetric irregular WBLs. The outline of this paper is as follows. The experimental conditions and some data analysis methodology are introduced in Section 2. Section 3 discusses the memory effect on boundary layer turbulence, Reynolds-averaged flow and bottom shear stress. The influences of wave irregularity on skewed and asymmetric irregular WBLs are presented in Section 4. Conclusions are provided in Section 5.

2. Experimental conditions and data analysis methodology

2.1. Experimental facility

Our experiments are conducted using the Wave-Current-Sediment (WCS) facility at the hydraulic lab of National University of Singapore. The WCS is essentially a U-shape OWT with a 10 m-long, 40 cm-wide and 50 cm-deep horizontal test section. A uniform oscillatory flow in the test section is generated by a hydraulic-driven piston located in a vertical cylindrical riser attached to one end of the test section. Thus, oscillatory flows equivalent to full-scale near-bed flows under coastal waves can be produced, except that the vertical wave orbital velocity is absent in the WCS. For simplicity we hereafter refer to these oscillatory flows as waves. Some previous studies, e.g. Yuan and Madsen (2014) and Yuan (2016), have demonstrated that the WCS can precisely generate the intended periodic or irregular waves, so the readers are referred to these publications for details on the WCS. Our experiments are conducted over two fixed rough bottoms, i.e. a sandpaper bottom and a marble bottom. They are created by gluing roughness elements onto flat aluminum plates, i.e. slip-resistant sandpaper tapes (physical roughness

height of about 1mm) and a mono-layer of 12.5mm-diameter ceramic marbles, respectively. Through a rigorous log-profile fitting analysis Yuan and Madsen (2014) obtained the theoretical bottom location $z = 0$ and equivalent Nikuradse sand grain roughness k_N for these two bottoms. For the sandpaper bottom, $z = 0$ is found to be 0.6 ± 0.1 mm below the mean crest level of bottom roughness elements and k_N is 3.7 ± 0.1 mm. For the ceramic-marble bottom, $z = 0$ is 4.0 ± 0.4 mm below the top of the marbles and k_N is 20 ± 3 mm. These results are directly adopted in this study.

2.2. Flow conditions

The free-stream velocity of irregular wave boundary layers are obtained by modifying a train of periodic waves as follows. Three periodic wave shapes are considered in this study, i.e. sinusoidal, skewed and asymmetric waves. The free-stream velocity for the latter two are given by the superposition of two harmonics

$$u_{p,\infty}(t) = U_{\infty 1} [\cos(\omega t) + \alpha \cos(2\omega t + \varphi_{\infty 2})] \quad (1)$$

where $\omega = 2\pi/T$ is the wave angular frequency with T being the wave period, $U_{\infty 1}$ is the amplitude of the first-harmonic velocity, α is the relative magnitude of the second-harmonic velocity, which should be less than 0.25 to avoid the occurrence of secondary peaks within one wave cycle, and $\varphi_{\infty 2}$ is the second-harmonic phase, which is 0 for skewed waves and $\pi/2$ for asymmetric waves. For non-breaking coastal waves, this two-harmonic approximation can reasonably capture the skewness and the asymmetry of bottom orbital velocity. In this study, the second-harmonic amplitude is fixed to be 1/5 of the first-harmonic velocity, i.e. $\alpha = 1/5$ in Eq. (1). As shown in Fig. 1, the

obtained nonlinear features are quite significant, e.g. the maximum velocity is 5/3 times the minimum velocity for skewed waves.

A simple way to introduce wave irregularity is modulating the amplitude of a periodic wave train, i.e.

$$u_{m,\infty}(t) = \frac{A - \cos \frac{2\pi}{T_r}t}{A + 1} u_{p,\infty}(t) \quad (2)$$

where T_r is the recursive period of the wave package and A is a modification factor. We hereafter refer to such irregular waves as modulated waves. The modification factor A is chosen to be 2, so the amplitude of the largest wave is three times that of the smallest wave. Fig. 2a shows the free-stream velocity of a modulated-wave sequence with the sinusoidal wave shape. Here an individual wave is defined as the oscillatory flow between two neighboring zero up-crossings of the free-stream velocity (the crosses in Fig. 2), so the modulation will only change the wave amplitude but keep the wave period. To avoid a significant change of the wave shape, the recursive period, T_r , is set to 30 times the wave period T for all modulated-wave sequences in this study. However, this also limits the wave irregularity, since the variation of wave amplitude is quite gradual due to the large number of waves within a recursive period. Therefore, it can be expected that individual waves within a modulated-wave test are very likely to behave as periodic waves. To enhance wave irregularity, another type of irregular-wave sequence is created by randomly recombining individual waves separated from a modulated-wave sequence (hereafter referred to as the random-wave sequence). Fig. 2b presents the random-wave sequence reconstructed based on the modulated-wave sequence in Fig. 2a. The irregularity is much more significant for the random waves, e.g. a large wave may follow a much smaller wave or vice versa (see

the waves highlighted in Fig. 2b). These two methods to generate irregular-wave sequences is not aimed at mimicking the boundary layer flows under a realistic sea state, e.g. in reality both wave period and wave shape can vary wave-by-wave and the wave amplitude should follow certain probability distribution. However, this does not defeat the main objectives of this study, i.e. investigating the memory effect and the influences of wave irregularity.

Our tests are conducted in pairs, i.e. a random-wave test is paired with its corresponding modulated-wave test. This allows us to identify an individual wave (e.g. W1 in Fig. 2) and compare its behaviors within the two tests, which can illustrate the memory effect. Also, a pair of tests will have the same wave period, same wave shape but different levels of wave irregularity, so a comparison of the experimental results between the paired two tests can elucidate the influences of wave irregularity on some physical quantities of interest, e.g. the TI-streaming. Three pairs of tests corresponding to three wave shapes are conducted over each rough bottom, so totally twelve tests are reported in this paper, which are summarized in Table 1. All tests have the same target RMS flow velocity ($u_{rms} = 1.05$ m/s), and the measured values listed in Table 1 are very close to the target. A single wave period, $T = 6.4$ s, is adopted, so the recursive period T_r for all tests is 192 s (30 waves per recurrence), The RMS Reynolds number defined as $Re_{rms} = u_{rms}A_{rms}/\nu$, where ν is the water kinematic viscosity and $A_{b,rms} = u_{rms}T/2\pi$, is about $1.4 \cdot 10^6$ for all tests, which is sufficiently high for ensuring prototype flow conditions. Based on the previous study of Yuan and Madsen (2014), our tests should be mostly within the fully-rough turbulent regime, expect for the smallest waves over the sandpaper bottom, so for simplicity the bottom

roughness k_b is taken as the Nikuradse equivalent sand grain roughness k_N in the following data analysis.

2.3. Velocity measurements

A two-dimensional Particle Image Velocimetry (PIV) system supplied by TSI Corporation is used for measuring bottom boundary layer flows in the plane of the lateral centerline of the facility. A double-pulsed YAG135-15 Litron Nano L laser produces a thin laser sheet through the transparent lid of the test section, which illuminates the near-bed flow seeded with tracing particles. A digital camera captures a pair of images of the target flow field with a short time interval, and the velocity measurements are eventually obtained through a cross-correlation analysis of the image pair. The system setup generally follows the previous study of Yuan and Madsen (2014), so the reader is referred to this paper for more details on the PIV system.

In all experiments, the vertical resolution of PIV measurement is about $60\mu\text{m}/\text{pixel}$, which is determined by the distance from measurement plane to the digital camera (roughly 1 m) and the camera lens' focal length (105 mm). A 128-by-16-pixel interrogation grid is adopted in the PIV cross-correlation analysis, and the algorithm reports a velocity vector in each quadrant of the interrogation grid. Thus, the horizontal and the vertical resolutions of velocity measurements are roughly 4 mm and 0.5 mm, respectively. For tests over the sandpaper bottom, a 2-mega-pixel (1600-by-1200) camera is used to allow a high sampling frequency (10Hz) and a vertical image coverage (about 70 mm) that is sufficient to cover the major part of the boundary layer. For the marble-bottom tests, since the boundary layer thickness is generally over 100 mm due to the larger bottom roughness, a 4-mega-pixel camera is adopted

to have a larger vertical coverage (about 120 mm) but a lower sampling rate (5Hz). Therefore, totally 64 and 32 samples per wave period are captured for tests over the sandpaper and the marble bottoms, respectively. The lowest level with valid PIV measurements is about 2 mm above the crests of roughness elements due to the bottom reflection of laser sheet. Limited by the memory of the PIV computer, a continuous measurement covers three 192-second recursive periods for all tests.

2.4. Data analysis methodology

Since the flow in the WCS is longitudinally uniform, the velocities measured at the same vertical level should be homogeneous, except for the instantaneous turbulence fluctuations. Thus, the measured 2D velocity field can be spatial- and ensemble-averaged into a Reynolds-averaged velocity profile

$$\langle \xi(z, t) \rangle = \frac{1}{MN} \sum_{m=1}^M \sum_{n=1}^N \xi(x_m, z, t + (n-1)T_r), 0 \leq t \leq T_r \quad (3)$$

where ξ is either the horizontal or vertical component of flow velocity (u, w), t is time, z is the vertical coordinate, x_i is the horizontal coordinate of the i -th velocity measurement of the total I velocity measurements at level z , and $N = 3$ is the number of recursive periods. The associated turbulence fluctuation is then given by

$$\xi'(x, z, t) = \xi(x, z, t) - \langle \xi(z, t) \rangle \quad (4)$$

Unless otherwise indicated, we will simply use $\xi(z, t)$ to denote the Reynolds-averaged quantities in the following text. The Reynolds stress normalized by water density is then obtained by calculating the covariance

$$\frac{\tau_R(z, t)}{\rho} = - \langle u'v' \rangle \quad (5)$$

where the operator $\langle \rangle$ is defined in Eq. (3). A turbulent intensity

$$k(z, t) = \langle u'^2 + v'^2 \rangle \quad (6)$$

is introduced to represent the strength of turbulence.

Many previous studies have demonstrated that the instantaneous Reynolds-averaged velocity profile of turbulent wave boundary layers follows a logarithmic law in the very near-bottom region. Thus, the bottom shear stress in this study is obtained through a log-profile fitting analysis, i.e. the shear velocity $u_*(t)$ is obtained by fitting the following distribution

$$u(z, t) = \frac{u_*(t)}{\kappa} \ln\left(\frac{z}{k_b/30}\right) \quad (7)$$

to the bottom-most five valid measurements at the instance t , where κ is the von Karman constant and k_b is the bottom roughness. The instantaneous bottom shear stress $\tau_b(t)$ is then obtained as

$$\tau_b(t) = \rho |u_*(t)| u_*(t) \quad (8)$$

This method is invalid during a short time window (about 30% of a wave period) around the flow reversals, since the occurrence of boundary layer separation due to a strong adverse pressure gradient, i.e. $\partial u_\infty / \partial t$ opposes u_∞ , leads to the absence of a logarithmic layer. Nevertheless, it still works as an interpolation for the gaps around flow reversals, when the actual bottom shear stress is believed to be close to zero. Yuan and Madsen (2014) have extensively discussed the validity of the log-profile fitting analysis and showed that it is the only valid method to infer bottom shear stress from PIV measurements for rough-bottom tests in the WCS.

3. Memory effect due to flow irregularity

For simplicity all the following discussions of the memory effect are based on the tests with the sinusoidal wave shape, since the same conclusions can be applied to other tests. Here we consider two typical individual waves in the two sandpaper-bottom tests (SIN1_s and SIN2_s), of which the free-stream velocities are highlighted as W1 and W2 in Fig. 2. In the random-wave test, W1 is a small wave, i.e. the amplitude of its free-stream first-harmonic velocity is $U_{b,1}=0.56\text{m/s}$, following a roughly three-times larger wave, while W2 is a large wave ($U_{b,1}=1.55\text{m/s}$) following a much smaller wave ($U_{b,1}$ is 0.48m/s). Since the memory effect depends on the change of wave condition, it can be studied by comparing these two waves in the modulated- and the random-wave tests. We shall start with the experimental results on turbulence, since the memory effect can be straightforwardly observed from the intra-period variation of some turbulence statistical values. Following this, the memory effect on Reynolds-averaged velocity and bottom shear stress are also discussed.

3.1. Memory effect on turbulence

Two turbulence statistical values, i.e. the turbulence intensity $k(z, t)$ and the Reynolds stress $\tau_R(z, t)/\rho$, are obtained from the PIV measurements. As discussed by Yuan and Madsen (2014), the PIV algorithm essentially filters out turbulence with a spatial scale smaller than the interrogation grid (of the order 1 mm) and a temporal scale shorter than the time interval between a pair of PIV images (of the order 100 μs). Thus, the obtained $\tau_R(z, t)/\rho$ and $k(z, t)$ are not quantitatively correct, but some qualitative conclusions

can still be made based on them.

3.1.1. Turbulence intensity

Fig. 3 presents the contour plots of turbulence intensity variation with time and distance to the bottom for the two selected waves, W1 and W2, over the sandpaper bottom. For waves within the modulated-wave test, as shown in Fig. 3 (c,d), the experimental results generally resemble those for periodic wave boundary layers, e.g. Sleath (1987) and Hay et al. (2012). Turbulences are mainly generated at the bottom, so the near-bottom turbulence intensity increases (decreases) during the acceleration (deceleration) stage of each half-period, and the peak values occur around the moment of peak free-stream velocity. Turbulence intensity generally decays as turbulences are diffused up to higher levels. Due to the low wave irregularity of the modulated-wave test, the contour plots in Fig. 3 (c,d) exhibit two almost identical lobes for the two half-periods, which should be expected for periodic sinusoidal wave boundary layers. Since the bottom-generated turbulence needs time to be diffused upward, during the initial stage of a wave cycle the flow at high levels is primarily controlled by the residual turbulence from the preceding wave cycle. As shown in Fig. 3e, the turbulences generated by the large preceding wave of W1 persist into W1's first half-cycle, which leads to very high turbulence intensities around the upper-left corner of the contour plot. The W2 wave follows a much smaller wave in the random-wave test, so before the arrival of its self-generated turbulence very weak residual turbulence occupies the high levels, making the upper-left corner of Fig. 3f almost white. Also, the turbulence intensity of W2's first half-cycle also seems to be reduced by the enhanced wave irregularity.

These experimental evidences clearly suggest that the memory effect at high levels can be quite significant during the first half-period due to the residual turbulences.

3.1.2. Reynolds stress

The experimental results on Reynolds stress echo those on turbulence intensity. As shown in Fig. 4 (a,b) the variations of Reynolds stress with time and vertical elevation for the two waves in the modulated-wave test are again similar to those observed for periodic wave boundary layers. Reynolds stress is produced near the bottom and diffused upward into the flow interior, and the peak Reynolds stress in the near-bottom region occurs almost in phase with the peak free-stream velocity. The positive and the negative lobes of Reynolds stress in the contour plot are almost identical due to the symmetry of the sinusoidal wave shape. Some memory effects can be clearly observed for the two waves in the random-wave test, as shown in Fig. 4 (c,d). For the W1 wave, very strong negative Reynolds stress left by the preceding wave controls the upper part of W1's boundary layer during most of its first half-cycle, while W1's self-produced positive Reynolds stress dominates in the very near-bed region. It seems that the strong overlying residual turbulences also enhances W1's positive Reynolds stress in the near-bed regime during the positive half-cycle, i.e. Fig. 4c has a darker near-bed red region than Fig. 4a. The difference between Fig. 4a and c during the negative half-period, i.e. the blue (negative) main lobe after $t/T = 0.5$, is quite negligible, indicating that the memory effect does not persist into the negative half-period. For the W2 wave shown in Fig. 4b, the memory effect due to a much smaller preceding wave leads to the absence of noticeable negative Reynolds stress at high levels

during the initial stage of the positive half-cycle, while the two main lobes in Fig. 4b are quite similar to those in Fig. 4d, except that the Reynolds stress within the positive (red) lobe is reduced slightly by the memory effect.

3.1.3. Near-bed turbulence

The near-bed turbulence is directly related to the bottom shear stress, and therefore is worth a close inspection. To better assess the memory effect on the near-bed turbulence, Fig. 5 presents the intra-period variation of turbulence intensity and Reynolds stress measured at the bottom-most level of valid PIV measurements ($z_{min} = 2.1$ mm). The footprint of the memory effect can be clearly observed for the W1 wave. When it is in the random-wave test (Fig. 5 (a,c)), the strong residual turbulence from the preceding wave dramatically increases the near-bed turbulence intensity until the flow reversal ($t/T \sim 0.5$). However, the effect on Reynolds stress is only noticeable before the peak free-stream velocity of the first half-cycle, i.e. the Reynolds stress is higher when W1 is in the random-wave test. For the W2 wave, the experimental results from the two tests are almost identical. This is because the strong self-produced bottom turbulence can quickly supersede the residual turbulence.

We can also make an overall assessment of the memory effect on the near-bed turbulence based on all waves in the two sandpaper-bottom tests (SIN1_s and SIN2_s). For each individual wave, we simply consider the period-averaged turbulence intensity

$$\bar{k}(z_{min}) = \frac{1}{T} \int_0^T k(z_{min}, t) dt \quad (9)$$

and the amplitude of the first-harmonic Reynolds stress, $\tau_{R1}(z_{min})/\rho$, ob-

tained from Fourier analyzing the intra-period variation of Reynolds stress at the bottom-most level $z_{min} = 2.1$ mm. Since all waves have the same wave period and bottom roughness, the wave condition can be represented by A_b/k_N , and therefore the measurements are plot against A_b/k_N in Fig. 6. As we can see, both $\bar{k}(z_{min})$ and $\tau_{R1}(z_{min})/\rho$ increase with A_b/k_N as expected. The agreement between the two tests are generally quite good, except for the turbulence intensities of the very small waves (low values of A_b/k_b). This is not supervising, because Fig. 5 already showed that even for the worst case (e.g. the W1 wave) the memory effect is only significant for the $k(z_{min}, t)$ during the first half-cycle. Therefore, we can conclude that the near-bed turbulence of an individual wave generally behaves as if the wave is within a periodic-wave train, despite of some limited memory effect at the beginning of a wave cycle.

3.2. Memory effect on Reynolds-averaged (RA) velocity

3.2.1. Velocity profiles

The instantaneous RA velocity profiles within a wave period generally exhibit the typical features observed for periodic wave boundary layer flows, e.g. when the free-stream flow is close its peaks, the boundary layer starts with a logarithmic distribution in the very near-bed region and then transits into the free-stream flow through an overshoot structure.

For the two typical waves, W1 and W2, discussed in the previous subsection, the memory effect on the instantaneous RA velocity is most significant during the acceleration stage of W1's first half-cycle, so some typical profiles of W1 are presented in Fig. 7. To facilitate the following discussions, we hereafter refer to the profiles from the modulated- and the random-wave

tests as M- and R-profiles (the dashed and the solid lines in Fig. 7), respectively. At the very beginning of W1, e.g. the instance P1 ($t/T = 3/64$), the difference between the two profiles is immaterial at the highest level of measurements, simply because of the same imposed free-stream velocity, but the R-profile's velocity becomes increasingly larger than that of the M-profile as the bottom is approached. At the bottom-most level, the difference is about a factor of 2. Given that W1 follows a much larger wave (hereafter named as W1p) in the random-wave test, this difference may suggest that at instance P1 the near-bed flow still “memorizes” the RA velocity of W1p. To demonstrate this, we identify W1p in the modulated-wave test (SIN1_s) and pick out its RA velocity profile at $t/T = 3/64$. This “ghost” profile is plotted in Fig. 7b (the red dots) for comparisons. As we can see, the difference between the R-profile and the “ghost” profile is only about 10% in the near-bed region, and the two profiles becomes much more diverged at higher levels due to the difference in free-stream velocity. These observations suggest that the flow memory can control the near-bed RA velocity during the initial stage of a wave cycle. As the flow continues into the W1's wave cycle, the memory effect quickly decays as the self-produced near-bed turbulence becomes dominant. As shown in Fig. 7c and d, the difference between the M- and the R-profiles becomes smaller at instance P2 ($t/T = 1/8$), and almost vanishes when the peak positive free-stream flow occurs, e.g. instance P3 ($t/T = 1/4$).

Many previous studies have shown that the first-harmonic velocity dominates the frequency spectrum for periodic sinusoidal oscillatory boundary layers. Thus, as an overall assessment of the memory effect over the entire wave period, we Fourier analyze the RA velocities of the two typical waves,

W1 and W2, in the two sandpaper-bottom tests (SIN1_s and SIN2_s) to get the amplitude $U_1(z)$ and the phase $\varphi_1(z)$ of their first-harmonic velocities. For simplicity, we again denote the profiles from the modulated- and the random-wave tests as M- and R-profiles, respectively. As shown in Fig. 8, these experimental results are highly similar to those obtained from periodic-wave experiments of Yuan and Madsen (2014). The U_1 profiles have overshoot structures, and φ_1 increases towards the bed, indicating that the near-bed flow leads the free-stream flow in phase. For both W1 and W2 waves, the difference between the R- and the M-profiles is very small in the near-bed region. In the region $z < 10$ mm, almost a perfect agreement between the two U_1 profiles of each wave is observed, and the difference in φ_1 is quite immaterial, i.e. the differences at the bottom-most level are only 3.5° and 1.3° for W1 and W2, respectively. This indicates that the memory effect on the near-bed RA velocity can be considered negligible, if the whole wave cycle is considered. Some slightly larger differences are observed at high levels. The overshoot of U_1 profile is larger when the wave is within the random-wave sequence. There is also some small difference in the free-stream velocities, which is probably due to the imperfect flow generation. Comparing the experimental results for W1 and W2, it seems that the memory effect on the RA velocity is more significant for a small wave following a large wave, which is in agreement with the experimental results on turbulence statistical values.

3.2.2. Boundary layer thickness

A characteristic wave boundary layer thickness, δ_m , is defined as the distance from the maximum overshoot of the U_1 profile to the bottom. Yuan and Madsen (2014) following van der A et al. (2011) calibrated the following

power-law formula for δ_m/k_b based on a collection of OWT periodic-wave experiments over rough bottoms

$$\frac{\delta_m}{k_b} = 0.079 \left(\frac{A_b}{k_b} \right)^{0.81} \quad (10)$$

where k_b is the bottom roughness, and A_b is the excursion amplitude of the free-stream flow. With a wave-by-wave analysis, we can obtain δ_m for all individual waves in the four tests with the sinusoidal wave shape (see Table 1), and compare the measurements with the formula predictions, which essentially represents the periodic-wave measurements from similar studies. As shown in Fig. 9, the data points gather into two data bands, i.e. a lower one containing measurements from the two marble-bottom tests (SIN1_m and SIN2_m) and an upper one containing measurements from the two sandpaper-bottom tests (SIN1_s and SIN2_s). No noticeable difference between the modulated- and the random-wave tests are observed, even for the small waves (the lower ends of data bands). Also, the agreement between our irregular-wave results and the predictive formula is very good, i.e. the data points distribute evenly on both sides of the solid line and nearly all points are within a factor of 1.2 (dashed lines) from the prediction. These results suggest that a wave boundary layer can be fairly developed within one wave cycle, so the boundary layer thickness is not sensitive to the memory effect.

3.3. Memory effect on bottom shear stress

The instantaneous bottom shear stress, $\tau_b(t)/\rho$, is obtained from log-profile fitting the instantaneous Reynolds-averaged (RA) velocity profiles in the very near-bottom region, so it can be expected that the memory effect on $\tau_b(t)/\rho$ should be similar to that on the near-bed RA velocity. Fig. 10

presents the obtained $\tau_b(t)/\rho$ for the two typical individual waves, W1 and W2, which have been extensively discussed so far. Markers are only shown for the phases when the instantaneous boundary layer has a reasonable near-bottom logarithmic region.

The comparison of $\tau_b(t)/\rho$ obtained from the modulated- and the random-wave tests clearly shows that the memory effect is most significant during the acceleration stage of W1's first half-cycle. Before the phase of peak free-stream velocity ($t = 1/4T$), the random-wave $\tau_b(t)/\rho$ (red dots) is larger than the modulated-wave $\tau_b(t)/\rho$ (black open circles) by 10-50%, which is in accordance with the observations in Fig. 7 that the near-bed RA velocity of W1 in the random-wave test is significantly enhanced due to the flow memory before the free-stream velocity reaches its first peak. This also agrees with the comparison for the near-bed Reynolds stress shown in Fig. 5c, i.e the random-wave Reynolds stress is much larger for $t < 1/4T$. The two measurements for the W2 wave shown in Fig. 10b are almost identical, so it can be concluded that the memory effect on bottom shear stress is only significant during the initial stage of small waves following big waves.

The measurements shown here also suggest that the maximum values and the intra-period variation of bottom shear stress are insignificantly influenced by the memory effect, so it is very likely that wave bottom shear stress can be modeled in a wave-by-wave manner. More discussions on this will be presented in Section 4.2.

4. Irregular wave boundary layers with flow skewness and asymmetry

In this section we present the experimental results for the tests with the skewed and the asymmetric wave shapes, i.e. the eight tests with pre-fix SKW and ASY in Table 1. For these tests, the memory effect discussed in the previous section is generally applicable, so this section focuses on the effects of wave irregularity on the boundary layer streaming and the intra-period variation of bottom shear stress, which are relevant to producing net sediment transport.

4.1. Boundary layer (TI-) streaming

Many previous OWT studies with velocity measurements have shown that a weak current $\bar{u}(z)$ is embedded in the strong skewed or asymmetric oscillatory flows, e.g. Ribberink and Al-Salem (1995) and van der A et al. (2011). In fact, $\bar{u}(z)$ is the residue after the cancellation of the TI-streaming $\bar{u}_s(z)$ and a balancing return current $\bar{u}_c(z)$ self-generated by the facility to ensure mass conservation, i.e.

$$\bar{u}(z) = \bar{u}_c(z) + \bar{u}_s(z) \quad (11)$$

If the direction of the enhanced half-cycle is taken as the positive direction, $\bar{u}_s(z)$ is negative and stronger than $\bar{u}_c(z)$ (positive) in the very near-bottom region, so $\bar{u}(z)$ starts with negative values close to the bottom and becomes positive at higher levels. Yuan and Madsen (2015) developed a predictive model for periodic turbulent oscillatory boundary layers in OWTs (see appendix A for key details). This model can separately predict $\bar{u}_s(z)$ and $\bar{u}_c(z)$,

which allows decomposing the predicted mean bottom shear stress, $\bar{\tau}_b$, into three components related to (1) the oscillatory flow, (2) the TI-streaming and (3) the facility-generated return current, as shown in Eq. (A.8). Yuan and Madsen (2015) showed that the first two components will always cancel each other, so $\bar{\tau}_b$ is solely due to the return current. Since $\bar{u}_s(z)$ have a comparable magnitude as $\bar{u}_c(z)$ (they largely cancel each other), and a larger $\bar{\tau}_b$ is associated with a stronger $\bar{u}_c(z)$, $\bar{\tau}_b$ can therefore indicate the strength of $\bar{u}_s(z)$. Their model predictions suggested that the TI-streaming of purely skewed waves are much stronger than that of comparable purely asymmetric waves, which is supported by the experimental results that $\bar{\tau}_b$ of purely skewed waves is much stronger. Therefore, we can use the measured $\bar{u}(z)$ and $\bar{\tau}_b$ to investigate the TI-streaming.

The mean current profile, $\bar{u}(z)$, is obtained by averaging the Reynolds-averaged velocity over a recursive period. Since our tests are conducted in pairs, i.e. each wave shape has two tests (modulated and random) with the same package of individual waves, we can compare their $\bar{u}(z)$ to see if the wave irregularity leads to some differences. As shown in Fig. 11, the general behavior of the measured $\bar{u}(z)$ follows what have been observed from periodic-wave tests. The magnitude of $\bar{u}(z)$ is very weak, i.e. less than 2.5 cm/s, and is negative from the bottom to roughly $z = 40\text{-}50$ mm. Comparing the measurements for each pair of tests, it can be clearly seen that the near-bed negative $\bar{u}(z)$ of a random-wave test is consistently weaker than that of the paired modulated-wave test. This implies that the TI-streaming is probably weaker for the random-wave tests. The experimental values of mean bottom shear stress, $\bar{\tau}_b$, listed in Table 2 further support this argu-

ment, i.e. $\bar{\tau}_b$ of the random-wave tests is consistently smaller. Thus, our experimental results suggest that the wave irregularity can reduce the TI-streaming. However, it should be noted that this conclusion may not be valid if the free-stream velocity, $u_\infty(t)$, of the random-wave tests is generated differently. In this study $u_\infty(t)$ of individual waves are cut out from the modulated-wave's $u_\infty(t)$ based on the zero up-crossings, so the memory effect will primarily influence the positive half-cycles and presumably will also modify the turbulence imbalance between the two half-cycles, which is the origin of the TI-streaming. If we were to cut out individual waves based on zero down-crossings, then the negative half-cycles would be subject to the primary memory effect. Since flow skewness or asymmetry differentiates the positive and negative half-cycles, the influence of memory effect may depend on which half-cycle goes first.

The wave-by-wave variation of TI-streaming in-principle can be investigated based on either the residual current $\bar{u}(z)$ or the mean bottom shear stress $\bar{\tau}_b$. Unfortunately the experimental error for $\bar{u}(z)$ of all tests and $\bar{\tau}_b$ of the asymmetric-wave tests are too large to yield meaningful wave-by-wave measurements, since they are very small signals that would require a large number of recursive periods to allow a small enough confidence limits. The experimental values of $\bar{\tau}_b$ for the skewed-wave tests, however, are sufficiently large (about 5-10% of the maximum bottom shear stress). Thus, we here discuss the wave-by-wave variation of TI-streaming based on the $\bar{\tau}_b$ of the four skewed-wave tests. Since there is no wave-by-wave variation of wave shape and wave period, a larger wave amplitude should lead to a stronger TI-streaming and hence $\bar{\tau}_b$. Thus, Fig. 12 plots the measured $\bar{\tau}_b$ versus the

amplitude of the first-harmonic free-stream velocity $U_{\infty,1}$, and each subplot compares a pair of tests with the same bottom condition. We also provide the results of four tests from Yuan and Madsen (2014), i.e. their tests ST200_ce, ST400a_ce, ST200_sa and ST400a_sa, which were conducted with the same rough bottoms used in this study. The wave shape and the wave period (6.25 s) of these tests very close to the individual waves in our skewed-wave tests, so we can directly plot them (the red crosses) in Fig. 12.

The data points clearly exhibit the expected trend that $\bar{\tau}_b$ increases with $U_{\infty,1}$, which suggests that in the presented tests the TI-streaming is able to response to the change of wave conditions. The modulated-wave tests (dots in Fig. 12) have quite low wave irregularity, so the wave-by-wave TI-streaming should behave as if the individual waves are within periodic wave trains. There is indeed a good agreement between the modulated-wave results and the periodic-wave results, despite that the data points are quite scattered and only two periodic-wave points are available for each bottom condition. If TI-streaming can immediately vary with the changing wave condition, we shall see no difference between the paired modulated- and random-wave tests, since they have the same basket of individual waves. However, a close inspection of the random-wave results (the open circles) suggest that their have smaller $\bar{\tau}_b$ for large wave conditions, i.e. the open circles are generally between the dots for $U_{\infty,1} > 120$ cm/s, but the opposite occurs for small wave conditions. This observation can be interpreted as follows. If a large wave in the random-wave tests follows a much smaller wave, its TI-streaming will have to be developed in a “start-from-scratch” manner, and consequently is less mature and weaker than when it follows a similar wave, which is the

situation in our modulated-wave tests. The opposite can be expected for small waves following large waves. Thus, we can say that the TI-streaming's response time can be longer than a wave period, depending on the wave irregularity. Nevertheless, the overall agreement between the two data clouds in each sub-figure of Fig. 12 is still good, indicating that the development of TI-streaming still can be mostly finished within a wave period, so the response time should not be much longer than a wave cycle.

The overall TI-streaming over the entire irregular wave package is insignificant affected by the wave irregularity (at least for the skewed-wave tests), as evidenced by the small difference in $\bar{\tau}_b$ (Table 2) and $\bar{u}(z)$ (Fig. 11) between a pair of tests. Therefore, if one were to wave-by-wave model the TI-streaming, the obtained overall streaming should be reasonably accurate. However, it is still questionable to wave-by-wave model the streaming-induced net sediment transport rate under irregular waves, since the response time of sediment concentration also plays an role.

4.2. Intra-period variation of bottom shear stress

Since the memory effect on bottom shear stress is quite limited, i.e. only the initial stage of a very small wave following a very large wave experiences some noticeable influence, the intra-period variation of bottom shear stress should display the key features that have been observed from periodic-wave studies. To demonstrate this, Fig. 13 presents segments (60-s long) of the obtained bottom shear stress together with the corresponding free-stream velocity for two sandpaper-bottom random-wave tests with the skewed and the asymmetric wave shapes (SKW2_s and ASY2_s), respectively. To facilitate the comparison, both quantities are normalized with their RMS val-

ues. The flow skewness enhances (reduces) the free-stream velocity during positive (negative) half-period, and therefore the obtained values of peak positive bottom shear stress in Fig. 13a are much larger. The intra-period variation of bottom shear stress also exhibits the skewness feature. For the asymmetric-wave test shown in Fig. 13b, the time series of the bottom shear stress resembles the asymmetric (forward-leaning) feature of the free-stream velocity, and the positive peaks are larger than the negative peaks in magnitude, which supports the argument that the shorter acceleration stage of the positive half-cycle leads to a thinner boundary layer and therefore larger bottom shear stress. For both tests shown in Fig. 13, the bottom shear stress clearly leads the free-stream velocity in phase, which is another well-known feature for wave bottom shear stress.

To further assess the effect of wave irregularity on the intra-period variation of bottom shear stress, we compare our experimental results with the periodic-wave results of Yuan and Madsen (2014). Their experimental setups are almost identical to this study, and their free-stream velocities are also given by the superposition of two harmonics, i.e. Eq. (1), except that their second-harmonic free-stream velocity is slightly larger, i.e. their α (relative magnitude of the second-harmonic free-stream velocity) is 0.25 (ours is 0.2). Yuan and Madsen (2014) shows that the time-varying bottom shear stress for periodic waves can be well approximated by the summation of the first three harmonics of its Fourier-series representation, i.e.

$$\tilde{\tau}_b(t) = \tau_{b,1} \cos(\omega t + \varphi_{\tau 1}) + \tau_{b,2} \cos(2\omega t + \varphi_{\tau 2}) + \tau_{b,3} \cos(3\omega t + \varphi_{\tau 3}) \quad (12)$$

where $\tau_{b,1}$ to $\tau_{b,3}$ are the amplitudes, $\varphi_{\tau 1}$ and $\varphi_{\tau 3}$ are the phase leads of the first and the third harmonics relative to the first-harmonic free-stream

velocity, respectively, and $\varphi_{\tau 2}$ is the phase lead of the second-harmonic bottom shear stress relative to the second-harmonic free-stream velocity. The amplitudes can be further expressed in terms of friction factors, i.e.

$$\begin{aligned}\tau_{b,1} &= \frac{1}{2}f_1\rho U_1^2 \\ \tau_{b,2} &= \frac{1}{2}f_2\rho\alpha U_1^2 \\ \tau_{b,3} &= \frac{1}{2}f_3\rho U_1^2\end{aligned}\tag{13}$$

Through a wave-by-wave analysis, we obtain these friction factors and the phase leads for our irregular-wave tests, and compare them with the results reported by Yuan and Madsen (2014). We also compare the experimental results with predictions yielded by the predictive model of Yuan and Madsen (2015). In Appendix A, the model predictions of friction factors and phase leads are further approximated with explicit formulas based on the relative roughness $X = A_b/k_b$ and the two parameters (α and $\varphi_{\infty,2}$) describing the second-harmonic free-stream velocity in Eq. (1). For a given wave shape, i.e. fixed values for α and $\varphi_{\infty,2}$, all friction factors and phase leads are single-variable functions of X , so the experimental results and the model predictions are separately presented for each wave shape in Figs. 14 (first harmonic) and 15 (second harmonic). The third-harmonic bottom shear stress is not shown here, as the conclusions are highly similar to the first harmonic, expect that the data is much more scattered. Three key observations can be made based on these two figures. Firstly, there is little data stratification between experimental results of the modulated- and the random-wave tests, i.e. the open-circles and the dots in all figures form overlapping data bands. Secondly, the irregular-wave results from this study agree very well with the periodic-wave results (red crosses). The friction factors from the periodic-wave tests

generally fall into the very narrow data bands of irregular-wave results. Only for f_2 under the skewed wave shape (Fig. 15a), the irregular-wave friction factors are slightly larger for $A_b/k_b > 100$ (the sandpaper-bottom tests), but the relative difference is only about 10%. The overall agreement for the phase leads are also quite good, despite of the much larger data scatter. Thirdly, the model reasonably predicts the leading two harmonics of bottom shear stress. For friction factors, the inaccuracy is generally within 5% for all f_1 predictions and f_2 for asymmetric waves. The model overestimates f_2 for the skewed wave shape by up to 20-30% for $A_b/k_b > 100$, which is actually because the explicit formulas are developed without considering the influence of TI-streaming, while the skewed waves have a quite sizable TI-streaming. For phase leads, the model moderately overestimates the phase leads by $5 \sim 15^\circ$. The inaccuracy may not be significant for predicting certain processes, e.g. energy dissipation due to bottom shear stress and sediment suspension. More discussions about the model performance are already provided by Yuan and Madsen (2015).

These observations show that wave bottom shear stress can almost immediately response to the change of wave condition and therefore can be modeled as periodic waves in a wave-by-wave manner.

5. Conclusions

In this study full-scale experiments of irregular wave boundary layers over rough bottoms are conducted in an OWT. Two types of irregular wave sequences, one obtained by modulating a periodic wave train and the other obtained by randomly re-combining individual waves, are adopted for a com-

parative study. The boundary layer flows are measured with a 2D PIV system, and the measurements are spatial- and ensemble-averaged to yield the Reynolds-averaged velocity and the turbulent fluctuations.

The memory effect, i.e. the local wave boundary layer flow receives some residual influence from the preceding wave, is investigated by comparing the experimental results of typical individual waves in the two irregular wave sequences. Both the measured turbulence intensity and Reynolds stress suggest that during the initial stage of a wave period, i.e. before the free-stream flow reach the first peak, the residual turbulence from the preceding wave dominates across the boundary layer, until the self-produced turbulence, which is originated from the bottom, becomes sufficiently strong. Therefore, the memory effect on turbulence is most significant for very small waves following very large waves, because the relatively strong residual turbulence can be dominant for a long period of time. Nevertheless, this effect does not seem to persist after the moment of the first peak free-stream velocity. Generally speaking, the memory effect does not severely affect the near-bed turbulence, which supports the observation that the wave bottom shear stress also experiences little memory effect. For the Reynolds-averaged velocity, the flow memory can make the instantaneous velocity profile closely resemble the continuation of the preceding wave at the very beginning of a wave cycle, but this effect vanishes very quickly. The experimental results on the first-harmonic velocity shows that the key spatial and temporal variations of Reynolds-averaged boundary layer flow are insignificantly influenced by the memory effect. This is also confirmed by the fact that the wave-by-wave boundary layer thickness closely follows the experimental results for periodic

wave boundary layers.

For irregular wave boundary layers with the skewed or the asymmetric wave shapes, a mean current is observed as in similar periodic-wave experiments. It is a residue after the cancellation of the TI-streaming and a facility-generated return current. The differences in this mean current between the modulated- and the random-wave tests suggest that wave irregularity slightly restricts the magnitude of the TI-streaming, which is supported by the measurements of the mean bottom shear stress. The wave-by-wave variation of the TI-streaming is investigated based on the wave-by-wave mean bottom shear stress. Experimental results suggest that the TI-streaming can respond to the change of wave condition in a fairly quick manner, so it can be more-or-less developed within one wave period. Thus, a wave-by-wave modeling of the TI-streaming seems to be plausible. The bottom shear stress of individual waves within irregular wave trains are highly similar to those observed from periodic-wave studies. The leading two harmonics of the bottom shear stress are compared to the experimental results from similar periodic-wave tests and also the model predictions of Yuan and Madsen (2015). Very good agreement between irregular-wave and periodic-wave measurements are observed, and the predictive model can accurately predict the magnitude (friction factors) of the bottom shear stress, and slightly overestimates the phase leads.

Some implications on modeling sediment transport under irregular coastal waves can be made based on our experimental results. The intra-period bed-load sediment transport rate reacts to the instantaneous bottom shear stress in a quasi-steady manner, since the response time of sediment grains to the change of bottom shear stress is much shorter than a wave period. Therefore,

bedload sediment transport rates under irregular waves can be modeled in a wave-by-wave or probabilistic manner, e.g. Holmedal and Myrhaug (2004), since we have shown that the wave irregularity has little effect on the intra-period variation of bottom shear stress. A similar conclusion can be made for modeling sediment pick-up rate at the bottom, which is also closely related to the time-varying bottom shear stress. However, the suspended sediment concentration, which is controlled by turbulence diffusion, may not timely react to the change of wave condition. For instance, the residual turbulence of a strong preceding wave enhance the sediment suspension for a weak following wave. Thus, the preliminary implication is that the probabilistic approach can be applied for predicting the bedload transport rate, but may not be suitable for predicting the suspended-load transport rate. Additional experiments over movable sand bottoms should be performed to further assess these implications.

Acknowledgments

The authors gratefully acknowledges the financial support from the start-up grant of National University of Singapore (WBS: R-302-000-089-133). The authors also thanks the CENSAM program for Singapore-MIT Alliance for Research and Technology (SMART) for providing the experimental facilities.

References

van der A, D.A., O'Donoghue, T., Davies, A., Ribberink, J.S., 2011. Experimental study of the turbulent boundary layer in acceleration-skewed oscillatory flow. *Journal of Fluid Mechanics* 684, 251–283.

- van der A, D.A., O'Donoghue, T., Ribberink, J.S., 2010. Measurements of sheet flow transport in acceleration-skewed oscillatory flow and comparison with practical formulations. *Coastal Engineering* 57, 331–342.
- van der A, D. A.and Ribberink, J.S., van der Werf, J., O'Donoghue, T., Buijsrogge, R., Kranenburg, W., 2013. Practical sand transport formula for non-breaking waves and currents. *Coastal Engineering* 76, 26–42.
- Abreu, T., Michallet, H., Silva, P.A., Sancho, F., van der A, D.A., Ruessink, B.G., 2013. Bed shear stress under skewed and asymmetric oscillatory flows. *Coastal Engineering* 73, 1–10.
- Bhawanin, M., O'Donoghue, T., Ribberink, J.S., 2014. Effect of flow irregularity on oscillatory boundary layer flow. *Proc. 34th International Conference on Coastal Engineering* , sediment. 44.
- Chassagneux, F.X., Hurther, D., 2014. Wave bottom boundary layer processes below irregular surfzone breaking waves with light-weight sheet flow particle transport. *Journal of Geophysical Research: Oceans* 119, 1668–1690.
- Fuhrman, D.R., Schler, S., Sterner, J., 2013. RANS-based simulation of turbulent wave boundary layer and sheet-flow sediment transport processes. *Coastal Engineering* 73, 151–166.
- Gonzalez-Rodriguez, D., Madsen, O.S., 2007. Seabed shear stress and bed-load transport due to asymmetric and skewed waves. *Coastal Engineering* 54, 914–929.

- Gonzalez-Rodriguez, D., Madsen, O.S., 2011. Boundary-layer hydrodynamics and bedload sediment transport in oscillating water tunnels. *Journal of Fluid Mechanics* 667, 48–84.
- Grant, W.D., 1977. Bottom friction under waves in the presence of a weak current: its relationship to coastal sediment transport. Ph.D. thesis. Massachusetts Institute of Technology. Cambridge, MA, U.S.
- Hay, A.E., Zedel, L., Cheel, R., Dillon, J., 2012. Observations of the vertical structure of turbulent oscillatory boundary layers above fixed roughness using a prototype wideband coherent doppler profiler: 2. turbulence and stress. *Journal of Geophysical Research: Oceans* 117(C3).
- Holmedal, L.E., Myrhaug, D., 2004. Bed load transport under irregular waves plus current from monte carlo simulations of parameterized models with application to ripple migration rates observed in the field. *Coastal Engineering* 51, 155–172.
- Holmedal, L.E., Myrhaug, D., 2006. Boundary layer flow and net sediment transport beneath asymmetrical waves. *Continental Shelf Research* 26, 252–268.
- Holmedal, L.E., Myrhaug, D., 2009. Wave-induced steady streaming, mass transport and net sediment transport in rough turbulent ocean bottom boundary layers. *Continental Shelf Research* 29, 911–926.
- Holmedal, L.E., Myrhaug, D., Rue, H., 2003. The sea bed boundary layer under random waves plus current. *Continental Shelf Research* 23, 717–750.

- Jensen, B.L., Sumer, B.M., Fredsøe, J., 1989. Turbulent oscillatory boundary layers at high reynolds numbers. *Journal of Fluid Mechanics* 206, 265–297.
- Jonsson, I.G., Carlsen, N.A., 1976. Experimental and theoretical investigations in an oscillatory turbulent boundary layer. *Journal of Hydraulic Research* 14, 45–60.
- Justesen, P., 1988. Prediction of turbulent oscillatory flow over rough beds. *Coastal Engineering* 12, 257–284.
- Kranenburg, W.M., Ribberink, J.S., Schretlen, J.J.L.M., Uittenbogaard, R.E., 2013. Sand transport beneath waves: The role of progressive wave streaming and other free surface effects. *Journal of Geophysical Research: Earth Surface* 118, 122–139.
- Kranenburg, W.M., Ribberink, J.S., Uittenbogaard, R.E., Hulscher, S.J.M.H., 2012. Net currents in the wave bottom boundary layer: On waveshape streaming and progressive wave streaming. *J. Geophys. Res.* 117, F03005.
- Longuet-Higgins, M.S., 1953. Mass transport in water waves. *Philosophical Transactions of the Royal Society of London. Series A, Mathematical and Physical Sciences* 245, 535–581.
- Madsen, O.S., 1994. Spectral wave-current bottom boundary layer flows. *Proc. 24th International Conference on Coastal Engineering* , 384–398.
- Myrhaug, D., 1995. Bottom friction beneath random waves. *Coastal Engineering* 24, 259–273.

- Myrhaug, D., Holmedal, L.E., Simons, R.R., MacIver, R.D., 2001. Bottom friction in random waves plus current flow. *Coastal Engineering* 43, 75–92.
- Myrhaug, D., Ong, M.C., Holmedal, L.E., 2015. Suspended sediments due to random waves including effects of second order wave asymmetry and boundary layer streaming. *Ocean Engineering* 104, 414–421.
- O’Donoghue, T., Wright, S., 2004. Flow tunnel measurements of velocities and sand flux in oscillatory sheet flow for well-sorted and graded sands. *Coastal Engineering* 51, 1163–1184.
- Ribberink, J.S., Al-Salem, A.A., 1995. Sheet flow and suspension of sand in oscillatory boundary layers. *Coastal Engineering* 25, 205–225.
- Ruessink, B.G., van den Berg, T.J.J., van Rijn, L.C., 2009. Modeling sediment transport beneath skewed asymmetric waves above a plane bed. *Journal of Geophysical Research: Oceans* 114, C11.
- Ruessink, B.G., Michallet, H., Abreu, T., Sancho, F., Van der A, D.A., Van der Werf, J.J., Silva, P.A., 2011. Observations of velocities, sand concentrations, and fluxes under velocity-asymmetric oscillatory flows. *J. Geophys. Res.* 116, C03004.
- Simons, R.R., Grass, T.J., Saleh, W.M., Tehrani, M.M., 1994. Bottom shear stresses under random waves with a current superimposed. *Proc. 24th International Conference on Coastal Engineering* , 565–578.
- Sleath, J.F.A., 1987. Turbulent oscillatory flow over rough beds. *Journal of Fluid Mechanics* 182, 369–409.

- Tanaka, H., Samad, M.A., 2006. Prediction of instantaneous bottom shear stress for smooth turbulent bottom boundary layers under irregular waves. *Journal of Hydraulic Research* 44, 94–106. doi:10.1080/00221686.2006.9521664.
- Trowbridge, J., Madsen, O.S., 1984. Turbulent wave boundary layers: 2. second-order theory and mass transport. *Journal of Geophysical Research: Oceans* 89(C5), 7999–8007.
- Yuan, J., 2016. Turbulent boundary layers under irregular waves and currents: Experiments and the equivalent-wave concept. *Journal of Geophysical Research: Oceans* 121, 2616–2640.
- Yuan, J., Madsen, O.S., 2010. On the choice of random wave simulation in the surf zone. *Proc. 32nd International Conference on Coastal Engineering*, waves.71.
- Yuan, J., Madsen, O.S., 2014. Experimental study of turbulent oscillatory boundary layers in an oscillatory water tunnel. *Coastal Engineering* 89, 63–84.
- Yuan, J., Madsen, O.S., 2015. Experimental and theoretical study of wave-current turbulent boundary layers. *Journal of Fluid Mechanics* 765, 480–523.

Figure captions

Figure 1. Normalized free-stream velocities of skewed and asymmetric waves.

Figure 2. Normalized free-stream velocity of irregular waves with the sinusoidal wave shape: (a) modulated waves (the dashed line is the normalized free-stream velocity of the entire recursive period, the crosses are zero up-crossings and the thick solid lines highlights two typical individual waves named as W1 and W2), (b) random waves (W1 and W2 waves are highlighted by the thick solid lines).

Figure 3. Turbulence intensity (T.I.) for two typical waves, W1 and W2 (see Fig. 2), over the sandpaper bottom (i.e. in tests SIN1_s and SIN2_s). The free-stream velocities for W1 and W2 are shown in (a) and (b), respectively. (c) and (e) are contour plots showing the turbulence intensity variation with height and time for W1 in the modulated and the random-wave tests, respectively. (d) and (f) are similar to (c) and (e) but for the W2 wave.

Figure 4. Reynolds stress for two typical waves, W1 and W2 (see Fig. 2), over the sandpaper bottom (i.e. in tests SIN1_s and SIN2_s). The free-stream velocities are shown in Fig. 3 (a, b). (a) and (c) are the contour plots showing Reynolds stress variation with height and time for the W1 wave, and (b) and (d) shows the same results for the W2 wave.

Figure 5. Intra-period variation of turbulence in the very near-bottom region for two typical waves, W1 and W2 (see Fig. 2), over the sandpaper bottom (i.e. in tests SIN1_s and SIN2_s): (a) and (b) show the turbulence intensity measured at the bottom-most level, $z_{min} = 2.1$ mm, (c) and (d) show the amplitude of first-harmonic Reynolds stress measured at z_{min} .

Figure 6. Wave-by-wave variation of the representative turbulence statistical values measured at the bottom-most level for tests with the sinu-

soidal wave shape ($z_{min} = 2.1$ mm for the sandpaper-bottom tests (SIN1_s and SIN2_s) and $z_{min} = 5.8$ mm for the marble-bottom tests (SIN1_m and SIN2_m)): (a) period-averaged turbulence intensity for individual waves, (b) amplitudes of the first-harmonic Reynolds stress for individual waves.

Figure 7. Instantaneous Reynold-averaged velocity profiles during the initial stage of the W1 wave (see Fig. 2) in the two sandpaper-bottom tests (SIN1_s and SIN2_s): (a) free-stream velocity, (b)-(d) velocity profiles (the red dots in (b) is the “ghost” velocity profile of the wave before W1 at phase P1).

Figure 8. First-harmonic velocity of the two typical waves, W1 and W2 (see Fig. 2), over the sandpaper bottom (tests SIN1_s and SIN2_s): (a) and (b) are the amplitude and phase profiles for the W1 wave, respectively, (c) and (d) are similar to (a) and (b), but for the W2 wave.

Figure 9. Boundary layer thickness versus A_b/k_b (open circles: measurements from the random-wave tests (SIN1_s and SIN1_m), dots: measurements from modulated-wave tests (SIN2_s and SIN2_m), solid line: a empirical formula based on some previous periodic-wave measurements, dashed lines: $\pm 20\%$ from the solid line).

Figure 10. Bottom shear stress for the two typical individual waves, W1 and W2, in tests SIN1_s (modulated) and SIN2_s (random).

Figure 11. Mean velocity profiles for tests with skewed or asymmetric wave shapes: (a) the two sandpaper-bottom tests with the skewed wave shape (SKW1_s and SKW2_s), (b) the two sandpaper-bottom tests with the asymmetric wave shape (ASY1_s and ASY2_s), (c) the two marble-bottom tests with the skewed wave shape (SKW1_m and SKW2_m) and (d) the

two marble-bottom tests with the asymmetric wave shape (ASY1_m and ASY2_m).

Figure 12. Wave-by-wave variation of mean bottom shear stress for skewed-wave tests (open-circles: random-wave tests, dots: modulated-wave tests, red crosses: periodic-wave tests from Yuan and Madsen (2014)): (a) tests over the sandpaper bottom (SKW1_s and SKW2_s) and (b) tests over the marble bottom (SKW1_m and SKW2_m).

Figure 13. Examples of free-stream velocity and bottom shear stress for the random-wave tests with flow skewness or asymmetry: (a) test SKW2_s and (b) test ASY2_s.

Figure 14. Friction factor and phase lead of the first-harmonic bottom shear stress (solid line: explicit formulas given in Appendix A, dots: measurements from modulated-wave tests, open circles: measurements from random-wave tests, red crosses: measurements from periodic-wave tests by Yuan and Madsen (2014)).

Figure 15. Friction factor and phase lead of the second-harmonic bottom shear stress (symbols are as in Figure 14).

Table 1: Summary of test conditions (u_{rms} is the measured RMS free-stream velocity, $U_{\infty,1,max}$ and $U_{\infty,1,min}$ are the amplitudes of the first-harmonic free-stream velocity of the largest and the smallest waves, respectively, and k_b is the bottom roughness)

Test ID	Irregularity	Wave shape	u_{rms} [m/s]	$U_{\infty,1,max}$ [m/s]	$U_{\infty,1,min}$ [m/s]	k_b [mm]
SIN1_m	modulated	sinusoidal	1.06	1.51	0.49	20.0
SIN2_m	random	sinusoidal	1.08	1.55	0.48	20.0
SKE1_m	modulated	skewed	1.07	1.50	0.49	20.0
SKE2_m	random	skewed	1.08	1.55	0.46	20.0
ASY1_m	modulated	asymmetric	1.07	1.49	0.49	20.0
ASY2_m	random	asymmetric	1.08	1.54	0.49	20.0
SIN1_s	modulated	sinusoidal	1.06	1.51	0.49	3.7
SIN2_s	random	sinusoidal	1.07	1.54	0.47	3.7
SKE1_s	modulated	skewed	1.08	1.49	0.49	3.7
SKE2_s	random	skewed	1.07	1.52	0.46	3.7
ASY1_s	modulated	asymmetric	1.06	1.49	0.48	3.7
ASY2_s	random	asymmetric	1.07	1.52	0.48	3.7

Table 2: Mean bottom shear stress for tests with the skewed or asymmetric wave shapes

Modulated-wave tests		Random-wave tests	
Test ID	τ_{bc} [cm^2/s^2]	Test ID	τ_{bc} [cm^2/s^2]
SKW1 _s	5.32	SKW2 _s	4.89
SKW1 _m	12.47	SKW2 _m	10.39
ASY1 _s	2.16	ASY2 _s	1.63
ASY1 _m	4.06	ASY2 _m	2.19

Figure 1:

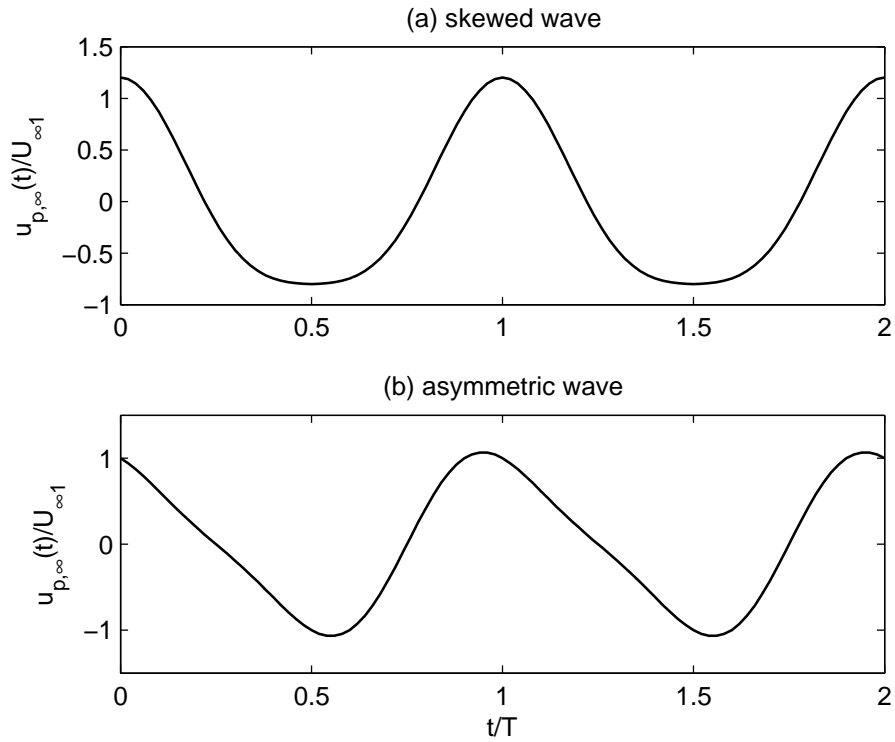


Figure 2:

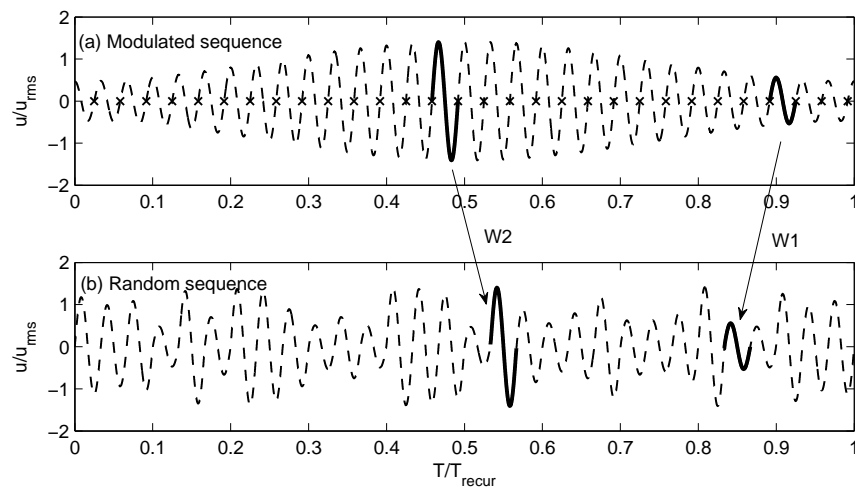


Figure 3:

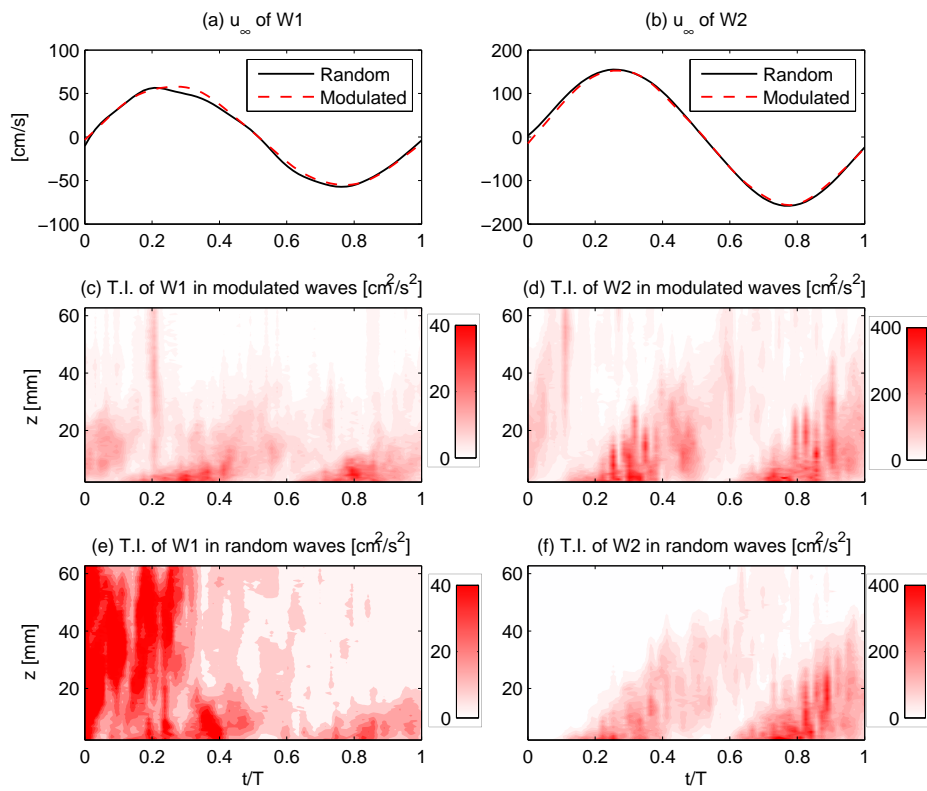


Figure 4:

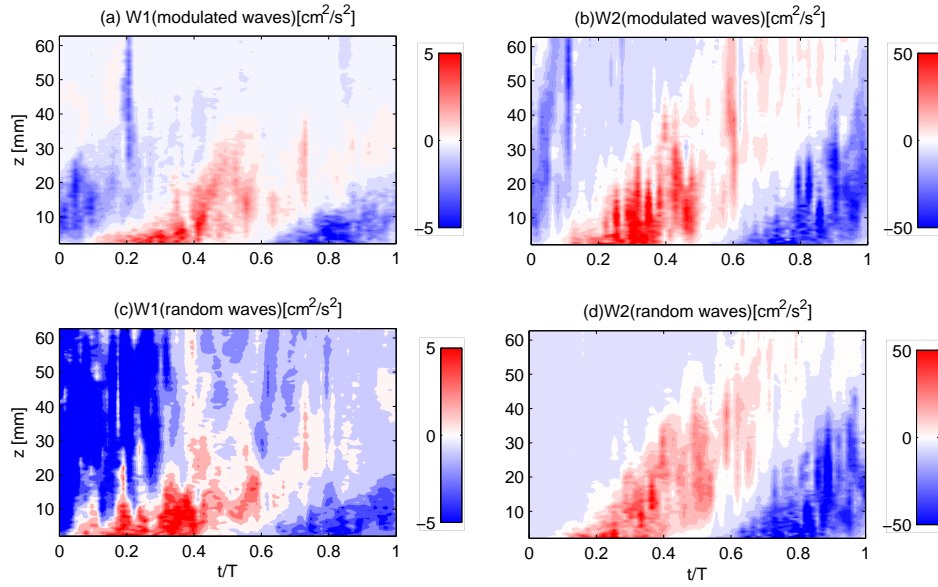


Figure 5:

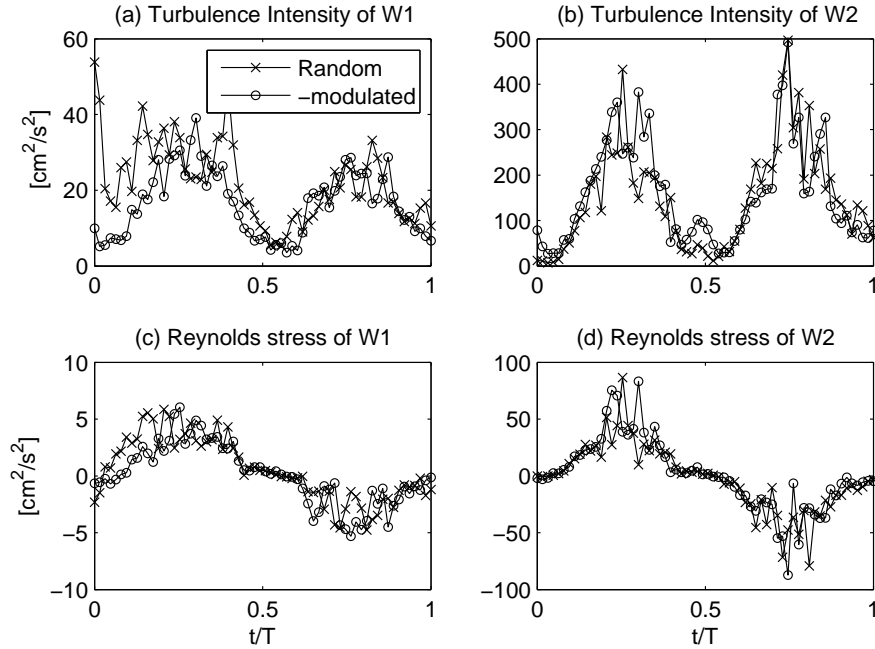


Figure 6:

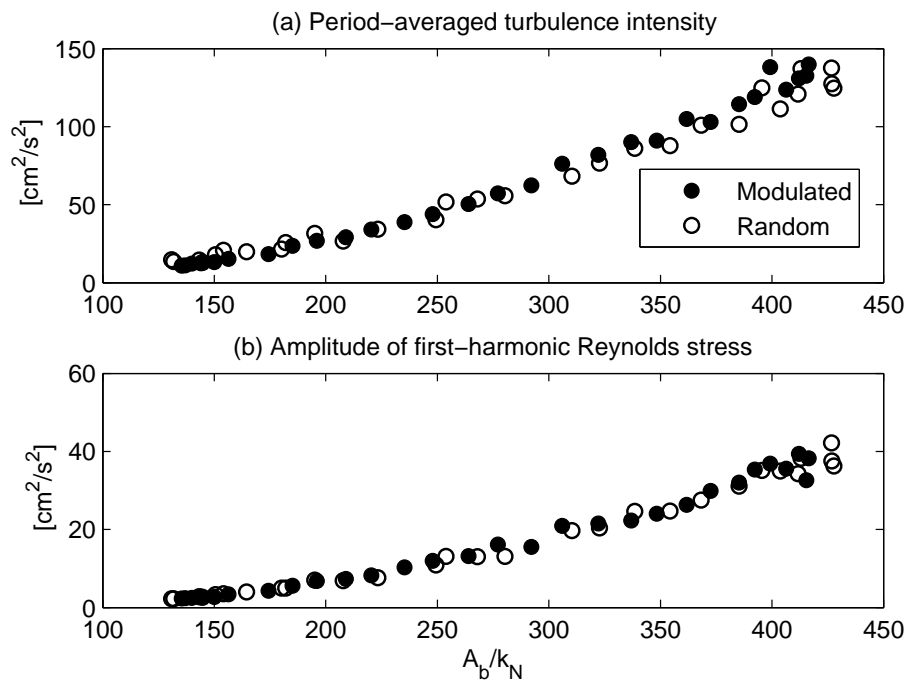


Figure 7:

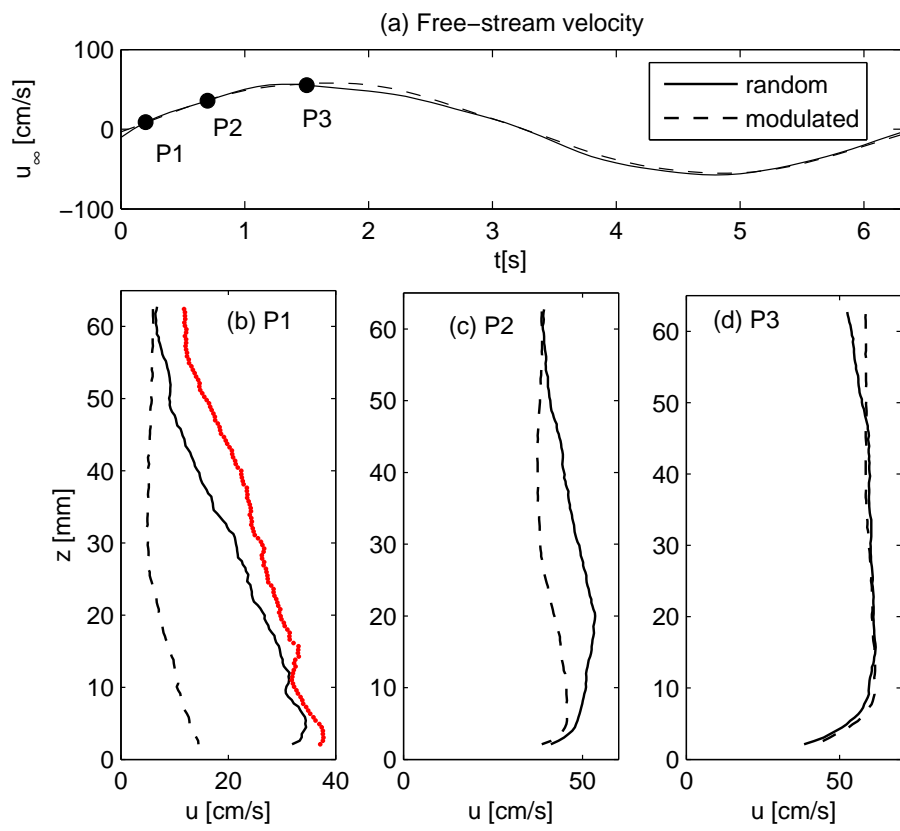


Figure 8:

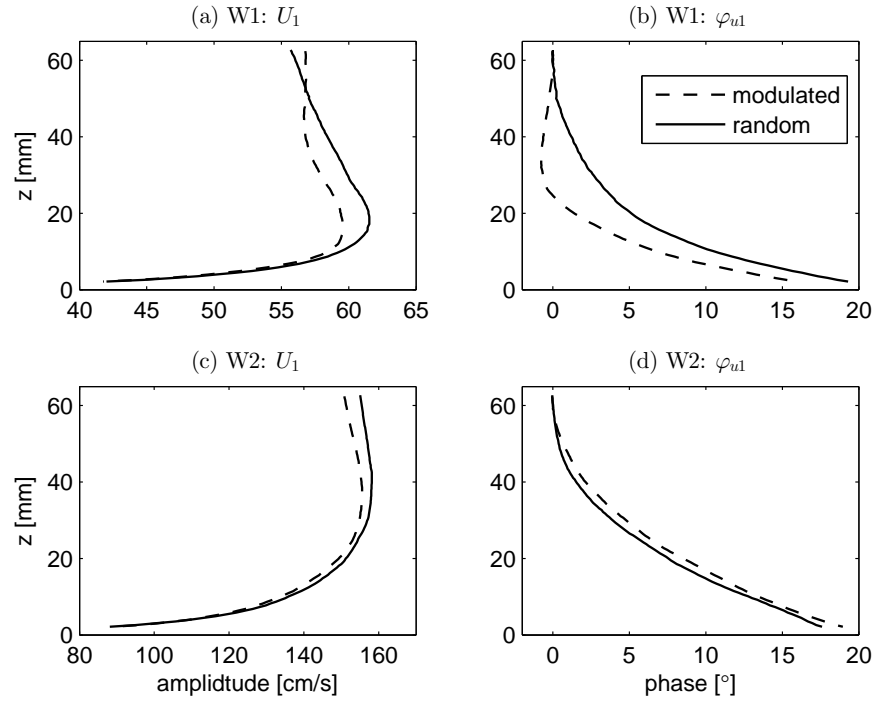


Figure 9:

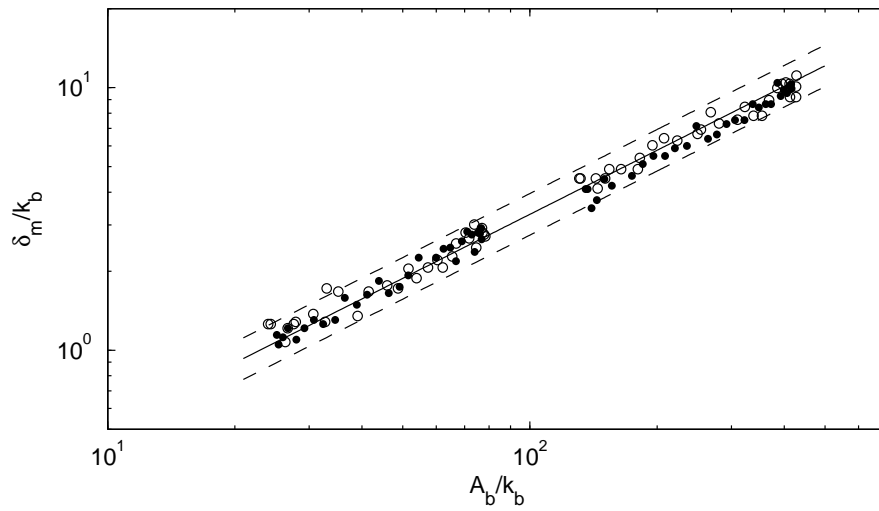


Figure 10:

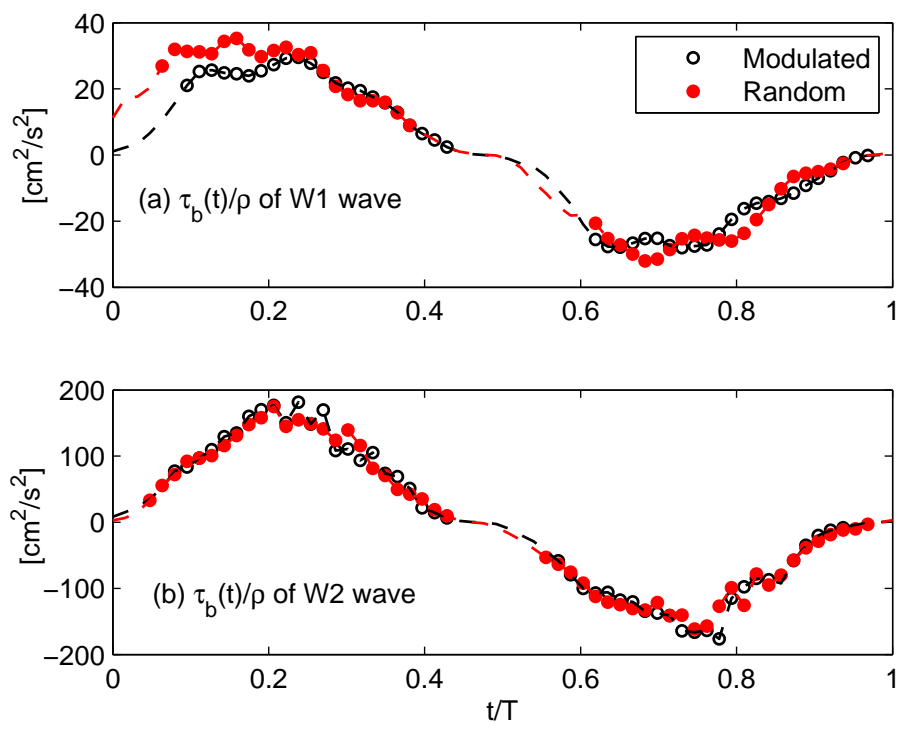


Figure 11:

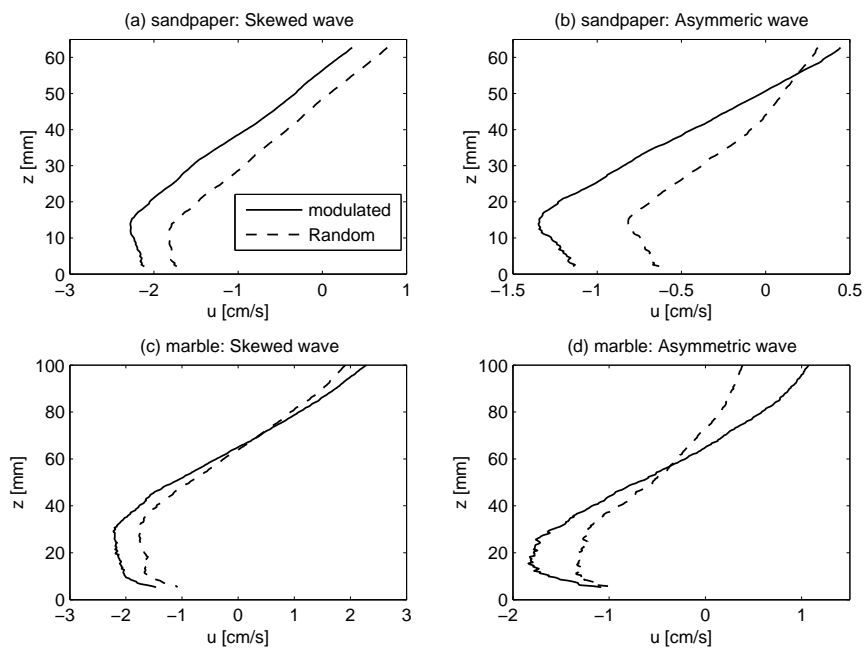


Figure 12:

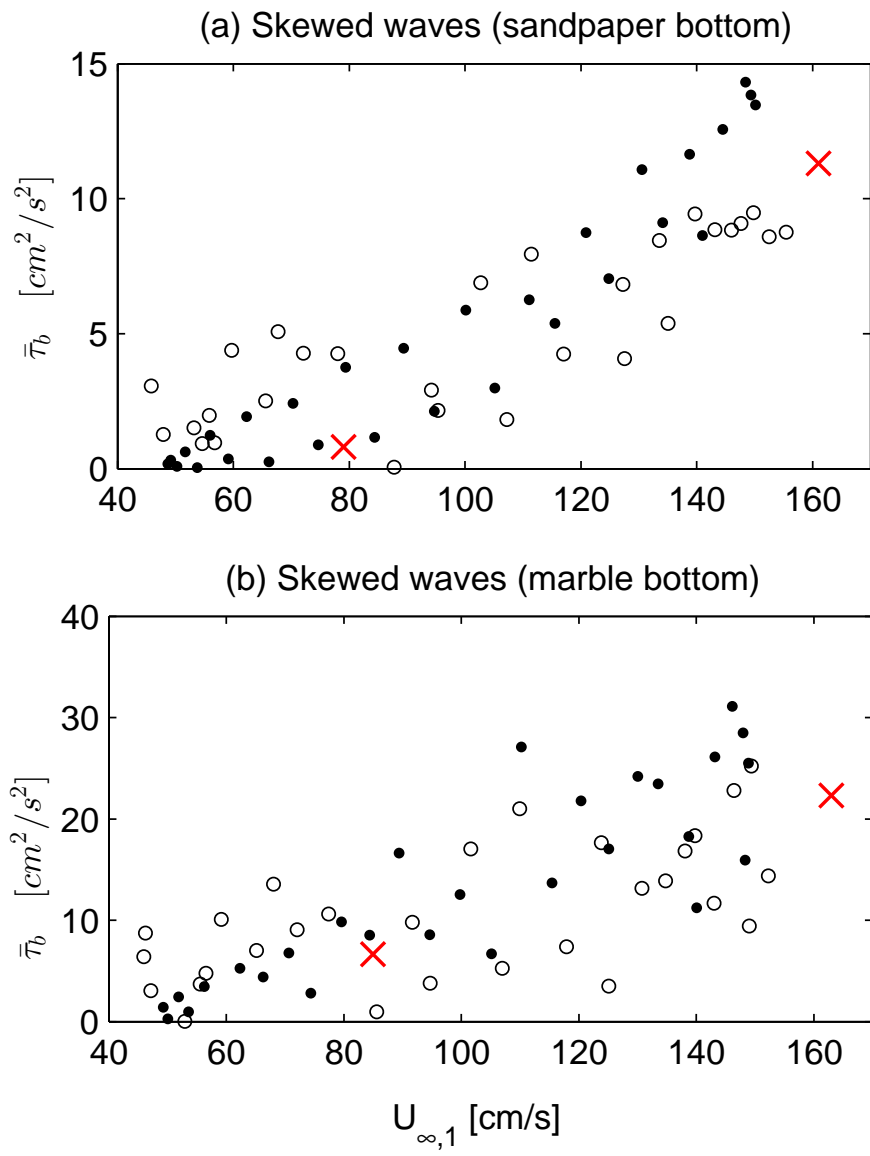
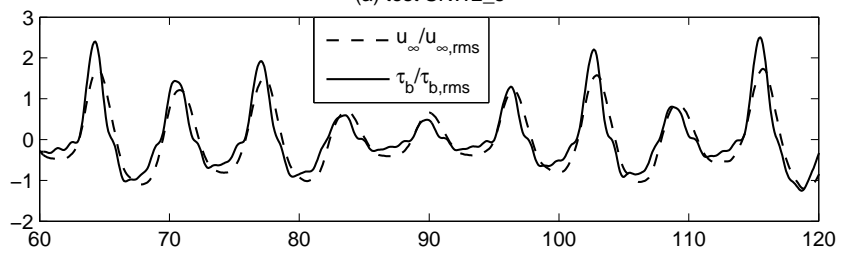


Figure 13:

(a) test SKW2_s



(b) test ASY2_s

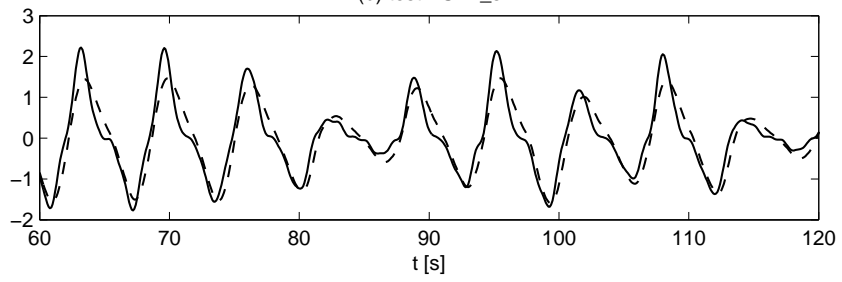


Figure 14:

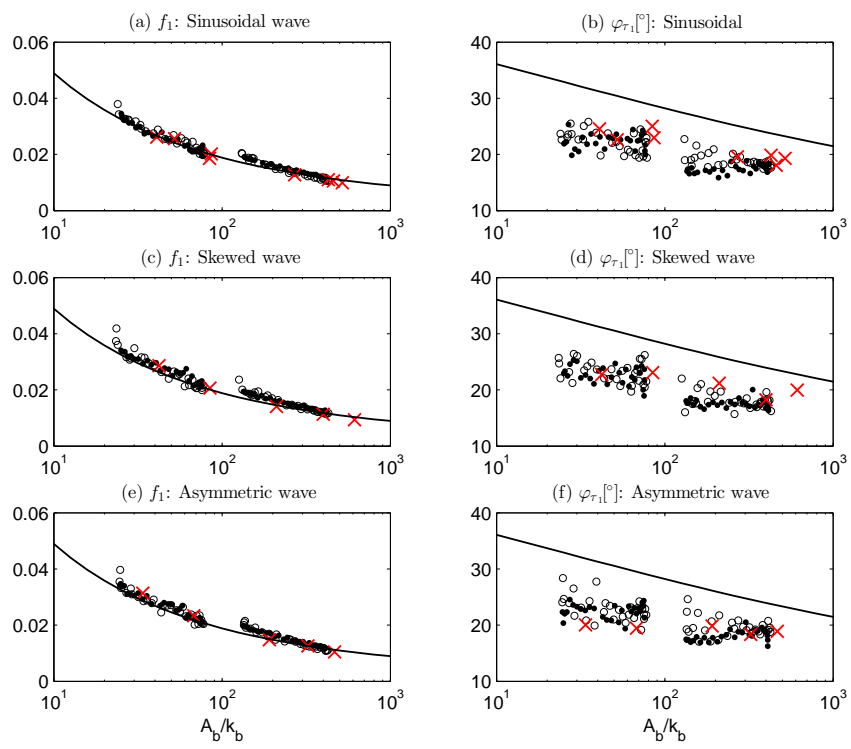
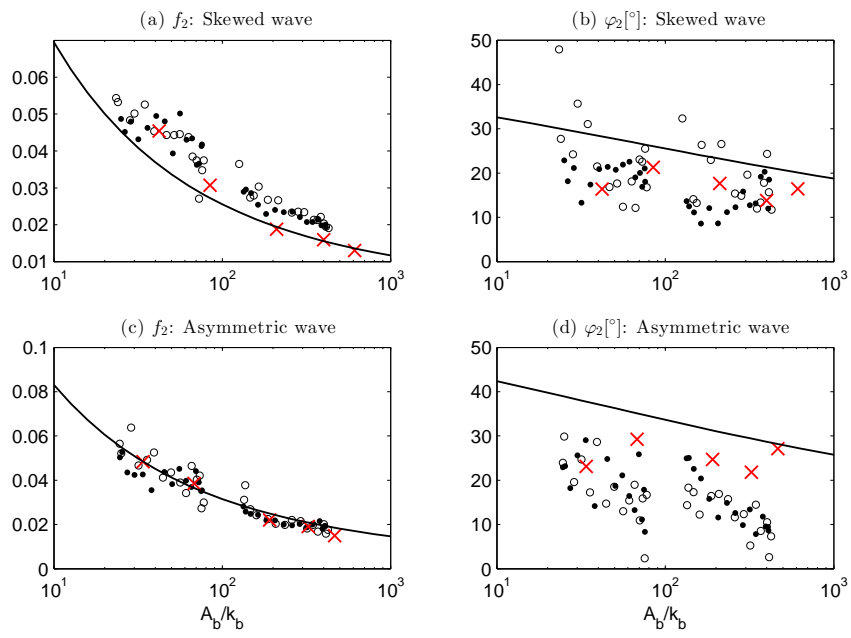


Figure 15:



Appendix A. Details of the Yuan and Madsen (2015)'s model

Yuan and Madsen (2015) developed a predictive model for periodic turbulent oscillatory boundary layers in the OWT. Due to the longitudinal homogeneity, the momentum equation is

$$\frac{\partial u}{\partial t} = -\frac{1}{\rho} \frac{\partial p}{\partial x} + \frac{\partial}{\partial z} \left(\frac{\tau}{\rho} \right) \quad (\text{A.1})$$

where u is the bottom-parallel Reynolds-averaged flow velocity, ρ is water density, t is time, p is water pressure, x and z are the bottom-parallel and bottom-normal coordinates, respectively, and τ is the Reynolds stress. Following the boundary-layer approximation, the pressure gradient term can be related to the free-stream velocity through

$$\frac{\partial u_\infty}{\partial t} = -\frac{1}{\rho} \frac{\partial p}{\partial x} \quad (\text{A.2})$$

where the free-stream velocity follows the two-harmonic expression, i.e. Eq. (1). The Reynolds stress is related to the z -gradient of flow velocity with a turbulent eddy viscosity

$$\frac{\tau}{\rho} = \nu_T \frac{\partial u}{\partial z} \quad (\text{A.3})$$

Following Trowbridge and Madsen (1984) and Gonzalez-Rodriguez and Madsen (2011), Yuan and Madsen (2015) expressed the time-varying turbulent eddy viscosity, ν_T as the product of a mean eddy viscosity and a temporal variation function

$$\nu_T(z, t) = \kappa u_{*wc} g(z) f(t) \quad (\text{A.4})$$

where κ is the von Karman constant, u_{*wc} is a characteristic shear velocity, $g(z)$ is the vertical variation function of the mean eddy viscosity and $f(t)$ is

a temporal-variation function. The boundary conditions for oscillatory flows

$$u = \begin{cases} u_\infty, z \rightarrow \infty \\ 0, z = z_0 = k_b/30 \end{cases} \quad (\text{A.5})$$

For a collinear superimposed current, the model only considers the near-bottom part of the current profile, so a depth-invariant mean shear stress is assumed. Thus, an analytical solution of current velocity is possible with the knowledge of a no-slip condition at $z = z_0$ and a reference current velocity at a reference level. In their model, the spatial-variation function $g(z)$ of $\nu_T(z, t)$ has an analytical four-layer structure, which can rigorously account for a variety of wave and current conditions, and $f(t)$ is approximated by a Fourier series. With the introduction of a new temporal variable, i.e.

$$\tau = \int f(t) dt \quad (\text{A.6})$$

the governing equation is first transformed into the τ -space, which can be solved analytically in a harmonic-by-harmonic manner. The analytical solution is then transformed back to t -space for matching the boundary conditions and also determining the model parameters through a closure, which requires the model predicts the bottom shear stress

$$u_{*wc}|f(t)| = \sqrt{\left|\frac{\tau_b(t)}{\rho}\right|} = \sqrt{\left|\nu_T \frac{\partial u}{\partial z}\right|_{z=0}} \quad (\text{A.7})$$

The back-transformation of analytical solution to t -space and the closure is conducted numerically, so the model is semi-analytical. By benchmarking against a variety of OWT experiments, including asymmetric or skewed oscillatory flows with or without a superimposed current, it is demonstrated

that the model can accurately predict the bottom shear stress, the Reynolds-averaged oscillatory velocity in the very near-bed region, the TI-streaming of skewed and asymmetric oscillatory flows and the current velocity profile under wave-current flows. A key advantage of this model is that it can separately predict the TI-streaming \bar{u}_s and the basic current \bar{u}_c , which allows the following decomposition of the mean bottom shear stress over a wave period

$$\frac{\bar{\tau}_b}{\rho} = \overline{[\nu_T(z, t) \frac{\partial \tilde{u}}{\partial z} + \bar{\nu}_T(z) \frac{\partial \bar{u}_s}{\partial z}]|_{z=z_0}} + \bar{\nu}_T(z) \frac{\partial \bar{u}_c}{\partial z}|_{z=z_0} \quad (\text{A.8})$$

where \tilde{u} is the wave velocity, $\bar{\tau}_b$ is the mean bottom shear stress and $\bar{\nu}_T$ is the mean turbulent eddy viscosity. The first two terms on the right-hand side are the mean bottom shear stress associated with the time-varying flow and the TI-streaming, respectively, and the last term is associated with a superimposed current. Yuan and Madsen (2015) shows that the first two terms will always cancel each other, so the mean bottom shear stress is solely due to the superimposed current.

In this study we are interested in the model prediction of the time-varying part of bottom shear stress, which can be approximated with the leading three harmonics, i.e. Eq. (12). The magnitudes of each harmonics can be further expressed as friction factors, i.e. Eq. (13). Model predictions suggest that the time-varying bottom shear stress can be obtained without considering a mean return current balancing the TA-streaming, so it can be shown that the friction factors and the phase leads of bottom shear stress are functions of three non-dimensional parameters, i.e. $X = A_b/k_b$ (relative roughness), α and the two parameters (α and $\varphi_{\infty,2}$) describing the second-harmonic free-stream velocity in Eq. (1). Therefore, it is possible to approximate the model predictions of f_1 to f_3 and φ_{τ_1} to φ_{τ_3} in Eq. (13) with explicit formulas

of these three parameters. Since the model assumes a flat bed, we only consider the predictions for $10 < X < 10^5$. Based on a sensitivity analysis, the first and the third harmonics of bottom shear stress are weakly affected by the second-harmonic free-stream velocity. Therefore, we express f_1 , f_3 , $\varphi_{\tau 1}$ and $\varphi_{\tau 3}$ as single-variable functions of X and obtain the following explicit formulas from fitting the exact model predictions

$$f_1 = \exp [5.670X^{-0.1045} - 7.475] \quad (\text{A.9})$$

$$f_3 = \exp [5.447X^{-0.1063} - 9.178] \quad (\text{A.10})$$

$$\varphi_{\tau 1}[\text{rad}] = 0.8095X^{-0.1198} + 0.0228 \quad (\text{A.11})$$

$$\varphi_{\tau 3}[\text{rad}] = 1.565X^{-0.1588} + 0.2846 \quad (\text{A.12})$$

The effect of skewness and asymmetry on bottom shear stress is primarily reflected by the second-harmonic bottom shear stress. A sensitivity analysis suggests that the influence of α on the second-harmonic friction factor f_2 is immaterial, so the following explicit formula for f_2 is obtained

$$f_2 = \exp [5.835X^{-0.1036} - 7.343 + \ln(0.15\varphi_{\infty 2}^{1.584} + 1)] \quad (\text{A.13})$$

For the second-harmonic phase, both α and $\varphi_{\infty, 2}$ are included in the explicit formula

$$\varphi_{\tau 2}[\text{rad}] = AX^{-0.1031} + B \quad (\text{A.14})$$

where

$$A = (0.22\alpha + 0.11)\varphi_{\infty 2}^2 + (-0.96\alpha + 0.06)\varphi_{\infty 2} + 0.64\alpha + 0.71 \quad (\text{A.15})$$

and

$$B = (0.26\alpha - 0.33)\varphi_{\infty 2}^2 + (-0.21\alpha + 0.51)\varphi_{\infty 2} - 0.13\alpha - 0.06 \quad (\text{A.16})$$

In all the explicit formulas $\varphi_{\infty,2}$ is in radians. All these explicit formulas are valid for $10 < X < 10^5$, $0 < \alpha < 0.25$ and $0 < \varphi_{\infty,2} < \pi/2$, and they deviate from the actual model predictions by less than 5% for the friction factors and 2° for the phase leads, which are smaller than the inaccuracy due to neglecting the mean flow in calculation.